If the skull fits: magnetic resonance imaging and microcomputed tomography for combined analysis of brain and skull phenotypes in the mouse

Brian J. Nieman, Marissa C. Blank, Brian B. Roman, R. Mark Henkelman and Kathleen J. Millen

Physiol. Genomics 44:992-1002, 2012. First published 4 September 2012;
doi: 10.1152/physiolgenomics.00093.2012

Physiological Genomics publishes results of a wide variety of studies from human and from informative model systems with techniques linking genes and pathways to physiology, from prokaryotes to eukaryotes. It is published 24 times a year (twice monthly) by the American Physiological Society, 9650 Rockville Pike, Bethesda MD 20814-3991. ESSN: 1531-2267. Visit our website at http://www.the-aps.org/.

Physiol Genomics 44: 992–1002, 2012.
First published September 4, 2012; doi:10.1152/physiolgenomics.00093.2012.

If the skull fits: magnetic resonance imaging and microcomputed tomography for combined analysis of brain and skull phenotypes in the mouse

Brian J. Nieman,[1,2] Marissa C. Blank,[3] Brian B. Roman,[4] R. Mark Henkelman,[1,2] and Kathleen J. Millen[5,6]

[1]*Mouse Imaging Centre, Hospital for Sick Children, Toronto, Ontario, Canada;* [2]*Department of Medical Biophysics, University of Toronto, Toronto, Ontario, Canada;* [3]*Department of Molecular Genetics and Cell Biology, University of Chicago, Chicago, Illinois;* [4]*Division of Biological Sciences, University of Chicago, Chicago, Illinois;* [5]*Center for Integrative Brain Research, Seattle Children's Hospital, Seattle, Washington; and* [6]*Department of Pediatrics, University of Washington, Seattle, Washington*

Submitted 5 July 2012; accepted in final form 30 August 2012

Nieman BJ, Blank MC, Roman BB, Henkelman RM, Millen KJ. If the skull fits: magnetic resonance imaging and microcomputed tomography for combined analysis of brain and skull phenotypes in the mouse. *Physiol Genomics* 44: 992–1002, 2012. First published September 4, 2012; doi:10.1152/physiolgenomics.00093.2012.—The mammalian brain and skull develop concurrently in a coordinated manner, consistently producing a brain and skull that fit tightly together. It is common that abnormalities in one are associated with related abnormalities in the other. However, this is not always the case. A complete characterization of the relationship between brain and skull phenotypes is necessary to understand the mechanisms that cause them to be coordinated or divergent and to provide perspective on the potential diagnostic or prognostic significance of brain and skull phenotypes. We demonstrate the combined use of magnetic resonance imaging and microcomputed tomography for analysis of brain and skull phenotypes in the mouse. Co-registration of brain and skull images allows comparison of the relationship between phenotypes in the brain and those in the skull. We observe a close fit between the brain and skull of two genetic mouse models that both show abnormal brain and skull phenotypes. Application of these three-dimensional image analyses in a broader range of mouse mutants will provide a map of the relationships between brain and skull phenotypes generally and allow characterization of patterns of similarities and differences.

craniofacial development; mouse phenotyping; mouse imaging; oculodentodigital dysplasia; Dandy-Walker malformation

THE DEVELOPMENT OF THE BRAIN and skull is an intricate and coordinated process that results in two complex structures fitting tightly together. Both physical and genetic factors participate in the direction of this process, and changes in either may result in an altered brain and/or skull morphometry. Characterization of such alterations, and of how brain and skull alterations relate to one another, will provide insight into the process of normal brain and skull development and into conditions where this development is perturbed.

It is recognized that the physical interaction between structures in the developing brain and skull can induce covariation in their shape (61). Premature fusion of a cranial suture, for example, results in an abnormal skull shape due to growth restriction in one direction (51). Brain growth is also physically constrained in these circumstances, and the brain is similarly altered in shape (5, 6, 77). Fear of increased intracranial pressure and abnormal craniofacial development motivates corrective surgery in these patients to partly normalize anatomical outcome (71). Furthermore, simple geometric measurements of the skull, such as the angle between the skull base and the front of the brain or landmarks on the facial bones, show a high degree of correlation with the total volume of the brain (16, 59, 81, 82). This observation seems to hold true in multiple species of mammals, a fact that informs some studies in anthropology and evolutionary science.

Brain and skull development are also controlled by common genetic factors (61). Such a dependence on genetics, as distinct from physical influences, is clear from co-occurrence of facial and limb phenotypes, as an example (76, 85), but also occurs in the brain and skull. Even in the case of craniosynostosis, morphological changes are observed throughout the brain, suggesting that additional genetic factors contribute to altered brain development (4, 77). Moreover, craniofacial abnormalities in mice have been generated by targeted (or random) manipulation of genes that impact skull development (52, 65, 97), including examples producing craniosynostosis (3, 63, 91), Down syndrome (7, 78), and cleft lip and palate (44, 72). Many of these genes were first identified (or have since been identified) as factors in related human conditions, and the genetic and phenotypic similarities between the two species provide a basis for probing the mechanisms of abnormal development and a means of testing novel interventions.

As the brain and skull develop simultaneously and, at least in the early stages, interdependently, it is not surprising that shape tends to correlate between the two. Holoprosencephaly is a notable example that has been appreciated for some time, wherein the degree of craniofacial phenotype is highly predictive of the underlying brain phenotype (33). Similarly, fetal alcohol syndrome produces characteristic facial phenotypes (28, 29) whose severity is predictive of the degree of mental disability (60) and changes in brain anatomy (83, 95) and which can be replicated in the mouse (8, 24, 70, 89). More recent work explores the possibility of more subtle connections between facial and brain phenotypes in autism spectrum disorder (2) and cleft lip/palate (93). It seems reasonable in cases showing a correspondence between brain and skull phenotypes to attribute the relationship to common physical and genetic interactions during development. However, there are also circumstances in which these phenotypes seem to diverge. In Dandy-Walker malformation, the posterior fossa tends to be larger than normal although the cerebellum contained within tends to be smaller (11), resulting in collection of cerebrospinal

Address for reprint requests and other correspondence: B. J. Nieman, Hospital for Sick Children, Mouse Imaging Centre, Toronto Centre for Phenogenomics, 25 Orde St., Toronto, ON, Canada M5T 3H7 (e-mail: bjnieman@phenogenomics.ca).

fluid in the unoccupied intracranial space. Developing an understanding of covariation in brain and skull features and the circumstances in which it becomes disrupted will be important in the study of many human conditions in which brain and craniofacial development are affected.

In addition to its significance in development and disease, the relationship between the brain and the skull is of interest in studies of anthropology and evolutionary science (77). In this case, the degree of brain development and its possible, albeit controversial (20, 50), implications for behavior and cognition are paramount, but direct fossil evidence of brain shape is rare and interpretation of individual specimens can be difficult (9, 47, 49). Fossil evidence of skull shape is more commonly available and therefore significant effort is made to interpret endocranial features and their ramifications for brain anatomy (48), and individual specimens may be considered at length (37–39, 62, 90). A long-standing theoretical question of whether brain reorganization or encephalization (i.e., the relative increase in the size of the brain) occurred first in evolutionary history persists, and its answer will depend critically on the relationship between the skull and the brain. Sophisticated tools for making measurements by hand (47) have been replaced largely by instruments permitting three-dimensional (3D) digitization (36) and by x-ray computed tomography (CT) (32, 79). The positions and relationships of prominent skull features (landmarks) provide a measure of shape, often using combinations of principal component or related analyses (41, 73, 99, 101), thin-plate splines (41, 80) or three-dimensional (3D) finite-element analysis (25) for morphometric analysis.

These evaluations allow shape comparisons between features or species. Comparison of ancient and modern hominid craniums has allowed inferences about shape changes over the course of evolution (17–19). The changes reveal that morphological features do not evolve in isolation, but in linked modules (26, 94), such that an elongated face, for instance, tends to be accompanied by characteristic changes in the cranial base (86). In a similar way, morphological comparisons between samples of various sizes indicates that shape is often size dependent, a property known as allometry (53). For example, an increase in the size of the neurocranium is generally accompanied by a proportionally larger increase in the size of the face (75, 80).

Study of shape over the course of development has revealed differences in the developmental process between species. For instance, the morphological trajectory of the human brain shows a prominent expansion of the parietal and cerebellar regions that doesn't occur in the chimpanzee (67). The human skull also changes shape through development, even after the brain has reached full size (13, 66). Morphological variability during growth provides a link between development and evolution (53, 54, 100, 101), and there is a common interest in identifying links between brain and skull shape and investigating what genetic changes alter this relationship.

The mouse is a particularly important model system for studying mammalian development. Morphological measurements of the brain and skull in mice can be linked directly to modified genetic factors. In previous work, mouse skull measurements have been made on the basis of manually identified landmarks in 3D images (26, 45, 46, 59, 78, 96, 100). Similar analyses have also been conducted in 3D images of the embryo (84) and the brain (7, 61, 73). We have also evaluated the morphometry of the brain and skull separately by computer-automated registration methods, which eliminate the need for manual identification of landmarks (68). While this approach may not be appropriate for very large phenotype differences, such as that between species, because it may become difficult for automated algorithms to meaningfully identify homologous points throughout the brain or skull, it does provide an efficient way of exploring brain-skull phenotype relationships in a variety of mouse models where the phenotypic changes are relatively small and the number of samples large.

In this work, we propose using combined magnetic resonance imaging (MRI) and microcomputed tomography (micro-CT) to evaluate the relationship between the 3D shapes of the brain and skull. This combination is meant to take advantage of the strengths of each imaging modality; MRI is known for excellent soft-tissue contrast, while CT is best suited for imaging of bone. Similar in concept to analyses that have been explored in other settings (6, 77), our analysis is designed to identify and compare brain and skull phenotypes. Our methods are tailored specifically for investigations in the mouse. We first characterize 3D differences between wild-type and mutant mouse groups separately in the brain and skull and then align the imaging results for comparison of these phenotypes. The predictive value of brain phenotypes in regions of statistically significant skull phenotypes is evaluated. We considered two mouse mutants to demonstrate our analysis, *Gja1*^{Jrt} (40) and *Zic1*$^{+/-}$;*Zic4*$^{+/-}$;*Shh*$^{+/-}$ (15), respectively, at adult and young adult ages. These mutants are models of oculodentodigital dysplasia (ODD) and of Dandy-Walker malformation (DWM).

MATERIALS AND METHODS

Mice. The *Gja1*^{Jrt} mutant mouse, modeling ODD, was generated by N-ethyl-N-nitrosourea (ENU) mutagenesis at the Centre for Modeling Human Disease (Toronto, ON, Canada) and has been described previously (40, 68). In brief, C57BL/6J male mice were treated with ENU and then bred with C3H/HeJ female mice. Offspring were bred to C3H/HeJ to test for heritability, and lines were maintained by breeding with C3H/HeJ females. Third-generation mice were used in these experiments, with unaffected littermates used as controls. Mice were fixed at ~60 wk of age for ex vivo imaging, with five mice in each the control and mutant groups. *Zic1*$^{+/-}$*Zic4*$^{+/-}$ (43) and *Shh*$^{+/-}$ mice, modeling DWM, were maintained on a 129S1/SvImJ background. Litter-matched and sex-matched *Zic1*$^{+/-}$;*Zic4*$^{+/-}$;*Shh*$^{+/-}$ mice and *Zic1*$^{+/+}$;*Zic4*$^{+/+}$;*Shh*$^{+/+}$ (9 of each) were killed at 38 ± 6 days of age (15). Image analyses and comparisons described below were all made between control and mutant images for the ODD and DWM separately.

All mouse imaging was performed ex vivo after intracardial perfusion fixation according to established protocols (87). Perfusion of saline and heparin was followed by 10% buffered formalin phosphate or 4% paraformaldehyde solution. A gadolinium-based contrast agent (Magnevist, Berlex Canada, or Prohance, Bracco Diagnostics) was included in the perfusate solutions (87, 102). *Zic1*$^{+/-}$;*Zic4*$^{+/-}$;*Shh*$^{+/-}$ specimens were further prepared for imaging by removing the extracranial tissue and soaking in 2 mM gadolinium-contrast solution for 7 days, allowing use of smaller, more sensitive solenoid coils for imaging. For both models, brain specimens remained within the skull to avoid distortions that may otherwise result from fixation and handling. All animal protocols were approved by the Hospital for Sick Children Animal Care Committee or by the Institutional Animal Care and Use Committee at the University of Chicago.

MRI. All MR images were acquired with a multiple-mouse MRI system and a Varian INOVA or DirectDrive console (Varian NMR

Instruments, Palo Alto, CA) and a 7.0-T magnet. Images of *Gja1*^{Jrt} mice were acquired with a 3D spin-echo sequence in 30 mm inner diameter millipede coils. Sequence parameters included 36 ms echo time (TE), 550 ms repetition time (TR), excitation tip angle 140°, 40 × 24 × 24 mm field-of-view, and 512 × 300 × 300 matrix size for an image resolution of 80 μm isotropic and an imaging time of 13 h 45 min. Images of *Zic1*$^{+/-}$;*Zic4*$^{+/-}$;*Shh*$^{+/-}$ mice were acquired with a 3D fast spin-echo sequence using 14 mm diameter solenoid coils. Sequence parameters included 30 ms effective TE, 10 ms echo spacing, 6 echoes, 325 ms TR, 4 averages, 25 × 12 × 12 mm field-of-view, and 780 × 432 × 432 matrix size for an image resolution of 32 μm isotropic and an imaging time of 11 h 20 min.

CT imaging. Micro-CT images of the *Gja1*^{Jrt} skulls were acquired using a MS-9 micro-CT scanner (GE Medical Systems, London, ON, Canada) with the x-ray source at 80 kV. Images were acquired in 2.5 h with 900 views and reconstructed on a 120 μm isotropic grid. Micro-CT images of the *Zic1*$^{+/-}$;*Zic4*$^{+/-}$;*Shh*$^{+/-}$ mouse skulls were acquired using a Triumph Tri-Modality system (Gamma Medica, Sherbrooke, QC, Canada) with the X-ray source at 75 kV. Three-dimensional images were reconstructed from 360 views to produce a 78 μm isotropic image.

Registration and structural analysis. *Gja1*^{Jrt} MRI, *Gja1*^{Jrt} CT, *Zic1*$^{+/-}$;*Zic4*$^{+/-}$;*Shh*$^{+/-}$ MRI, and *Zic1*$^{+/-}$;*Zic4*$^{+/-}$;*Shh*$^{+/-}$ CT image sets were initially registered together independently for each modality and genotype (combining the control and mutant *Gja1*^{Jrt} together in one space and the control and mutant *Zic1*$^{+/-}$;*Zic4*$^{+/-}$;*Shh*$^{+/-}$ together in another space). All the registrations (linear and nonlinear) were performed with tools from the Montreal Neurological Institute (30). The registration procedure commenced with rigid body registration (which includes three translation and three rotation parameters) to a pre-existing atlas to define orientation. Subsequently, to define an unbiased space independent of the atlas, all pairwise affine registrations between images in the data set were performed and used to compute an average linear transform for each image. Each average transform was applied to its respective image and all resultant images were intensity averaged to generate an unbiased (linear) average. Subsequently, images were registered nonlinearly toward the population average, and these results used to generate a refined average. This process was repeated iteratively at progressively finer deformation resolutions. At the final stage, affine linear transformations were removed from the final deformation fields using a mask over the analysis region of interest to produce a purely linear and a purely nonlinear deformation field for each image. The separation of the deformation field into these two components is convenient because it allows morphological changes to be analyzed with or without the effects of bulk volume change as needed. The unbiased average was adjusted to ensure it was centered on all deformation fields. These registration procedures and analyses have been described in numerous previous publications (23, 34, 55, 58, 68, 87). The end result of this process provides a complete set of nonlinear transforms that bring each image to an unbiased average space with all brain or skull structures in register.

Volumetric changes were computed on the basis of the deformation field results. Volumetric changes were first evaluated by calculating the determinant of the Jacobian matrix (a matrix whose elements are the first-order partial derivatives of each vector component of the deformation field, which here included both linear and nonlinear parts) at each voxel (3D pixel) in the image. This represents the voxel volume change as a ratio between the volume of the voxel after transformation to the original volume. All comparisons were made between *Gja1*^{Jrt} mice and their littermate controls, or between mutant *Zic1*$^{+/-}$;*Zic4*$^{+/-}$;*Shh*$^{+/-}$ and control *Zic1*$^{+/+}$;*Zic4*$^{+/+}$;*Shh*$^{+/+}$ mice (and not between *Gja1*^{Jrt} and *Zic1*$^{+/-}$;*Zic4*$^{+/-}$;*Shh*$^{+/-}$ mice). For further analysis of brain images, a segmented atlas (34) consisting of 63 structures was registered to the final unbiased average image. This matched existing segmentations from the atlas to the average images of interest. Measurement of brain structure volumes was then achieved by integration over the determinant of the Jacobian matrix for each structure and for each image in the data set. Comparisons of the volumetric results were made between mutant and control images. We have used this atlas-based analysis previously to detect subtle phenotypes in the mouse brain including sex-specific (87) and lateral asymmetries (88) and in various mutant mice (22, 35, 98). As with voxelwise analysis, all structure volume comparisons were made between *Gja1*^{Jrt} mice and their controls, or between *Zic1*$^{+/-}$;*Zic4*$^{+/-}$;*Shh*$^{+/-}$ and their controls.

Intermodality registration and analysis. To align images of the brain with images of the skull for both genotypes, bone-like images were synthesized from the MRI unbiased average images for registration with the CT unbiased average images. The bone-like images were produced by reversing the MRI color scale (i.e., switching black and white intensities) and then masking out the brain and extracranial tissue around the skull. Affine registration to the CT average images produced a transform between the MRI and CT spaces. MRI data and deformation fields were then transformed into the respective CT spaces to bring all images for a given genotype (with respective control images) into a common space.

To visualize the CT results and to compare the deformation fields on the surface of the brain with those on the inside of the skull, we computed components of the deformations perpendicular to and in the plane of the skull (Fig. 1). For this purpose, streamlines across the skull were computed on the basis of Laplace's equation solved between segmentations of the intracranial and extracranial space, identical to an algorithm described elsewhere for evaluating cortical thickness (56). The vector pointing from the intracranial space

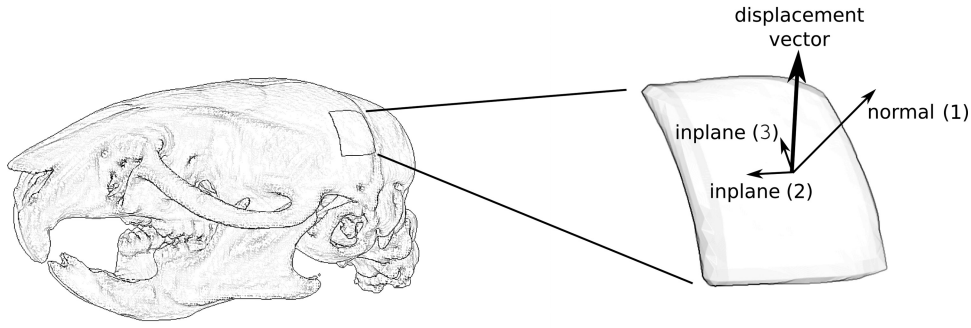

Fig. 1. Schematic showing the decomposition of displacement vectors on the skull. A sketch of the outside of the skull surface is shown at *left*. At each location on the surface (square at *left*, expanded at *right*), the normal vector pointing out of the skull surface was defined. Displacements resulting from the registrations were then separated into 3 components: *1*) displacements along the skull normal vector; *2*) displacements both in the plane of the skull (that is, perpendicular to the normal vector) and pointing in the rostral-caudal direction [labeled as inplane (1) at *right*]; and *3*) the residual displacements (perpendicular to each of the previous two vectors and thus including left-right and dorsal-ventral components in the plane of the skull). The first 2 of these, the normal component and the rostral-caudal in-plane component, are presented in detail in subsequent figures for both *Gja1*^{Jrt} and *Zic1*$^{+/-}$;*Zic4*$^{+/-}$;*Shh*$^{+/-}$ mice.

toward the extracranial space was taken as the local definition of the skull surface normal vector and used to resolve the deformation fields into three components: *1*) displacement normal to the skull surface, *2*) displacement in the plane of the skull and in the rostral-caudal direction, and *3*) the residue both in the plane of the skull and in the left-right or dorsal-ventral direction.

Statistical testing. Structural volume results for MRI data, voxelwise Jacobian data (more precisely, the logarithm of the Jacobian matrix determinant), and normal and in-plane vector displacements were compared with Student's *t*-tests, independently for each mutant with its respective control group. To compare complete vector displacements, we computed the Hotelling's T^2 field (21, 68) and then visualized results in significant regions using the magnitude of the average vector displacement between the mutant and control groups. The Hotelling's T^2 field is related to the F-distribution by a multiplicative scale factor, so statistical testing was achieved with an F-test. All statistical tests were corrected for multiple comparisons using the false discovery rate (FDR) (14), which ensures that, on average, no more than a specified percentage of positive results will be false positives (and which is a more stringent statistical test than $P < 0.05$). Description of the FDR algorithm and of its use in image analysis in particular has been described elsewhere (42).

We modeled skull surface displacements as a function of brain surface displacement, brain structure volumes, and genotype. To determine which factors were most important, we performed analysis of variance with an F-test after adding additional model terms (starting with the factor that accounted for the greatest variance). The same procedure was used to evaluate brain volume and genotype as explanatory variables for intracranial volume derived from CT. The predictive analyses are correlative in nature, so the modeling of CT skull displacements by MR brain displacements or volumes is not intended to suggest the latter are causative but, rather, establishes a relationship in the shape of the different features.

RESULTS

$Gja1^{Jrt}$ and $Zic1^{+/-};Zic4^{+/-};shh^{+/-}$ show morphometric brain phenotypes. We compared the brain structure of *$Gja1^{Jrt}$* and *$Zic1^{+/-};Zic4^{+/-};Shh^{+/-}$* mice with their respective control mice using high-resolution MRI of fixed mouse brains. We measured local changes in brain volume between the control and mutant mouse images at each voxel. Both *$Gja1^{Jrt}$* and *$Zic1^{+/-};Zic4^{+/-};Shh^{+/-}$* mouse mutants, respectively, models of ODD and DWM, showed significant abnormalities in structures throughout the brain (Figs. 2 and 3, respectively). Structural volume changes were also evaluated for 63 brain structures (34). Each of the mutants showed a total of 37 significantly different structure volumes. However, of the 37 structures identified as abnormal in each of the mutants, 24 structures were common between them, and 13 differed. Select structure volumes are plotted in Figs. 2 and 3.

$Gja1^{Jrt}$ and $Zic1^{+/-};Zic4^{+/-};shh^{+/-}$ show morphometric skull phenotypes. We next compared the skull structure of the *$Gja1^{Jrt}$* and *$Zic1^{+/-};Zic4^{+/-};Shh^{+/-}$* mice to their associated controls using micro-CT. The first two of the directional displacements defined in Fig. 1 proved to be of greatest interest for the mutants examined here. The magnitude of vector

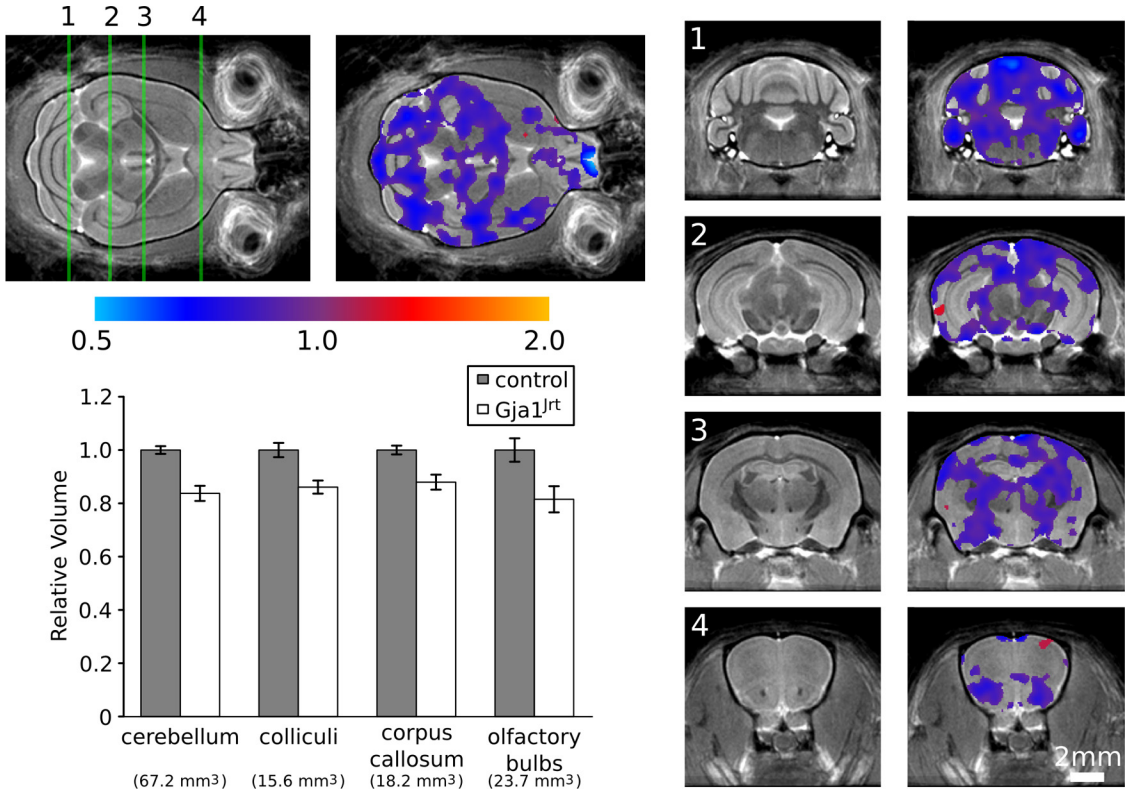

Fig. 2. MRI-detected brain phenotypes in the *$Gja1^{Jrt}$* mouse. Voxelwise volumetric changes (where FDR <0.05) are shown overlaid on the unbiased average image (shown without overlay at *left* for each slice). Blue corresponds to decreases in size for the mutant and red to increases. Horizontal images (*top left*) include green lines indicating the location of the coronal slices (shown at *right*). Integration of voxelwise volume changes over segmented structure volumes provided a measure of volumetric changes. Thirty-seven (37) structures of the 63 tested showed significant differences (FDR <0.05). Four structures of interest are shown in the bar graph (*bottom left*) with error bars showing standard SE. Volumes are shown normalized to the average control volume for each structure (shown in parentheses).

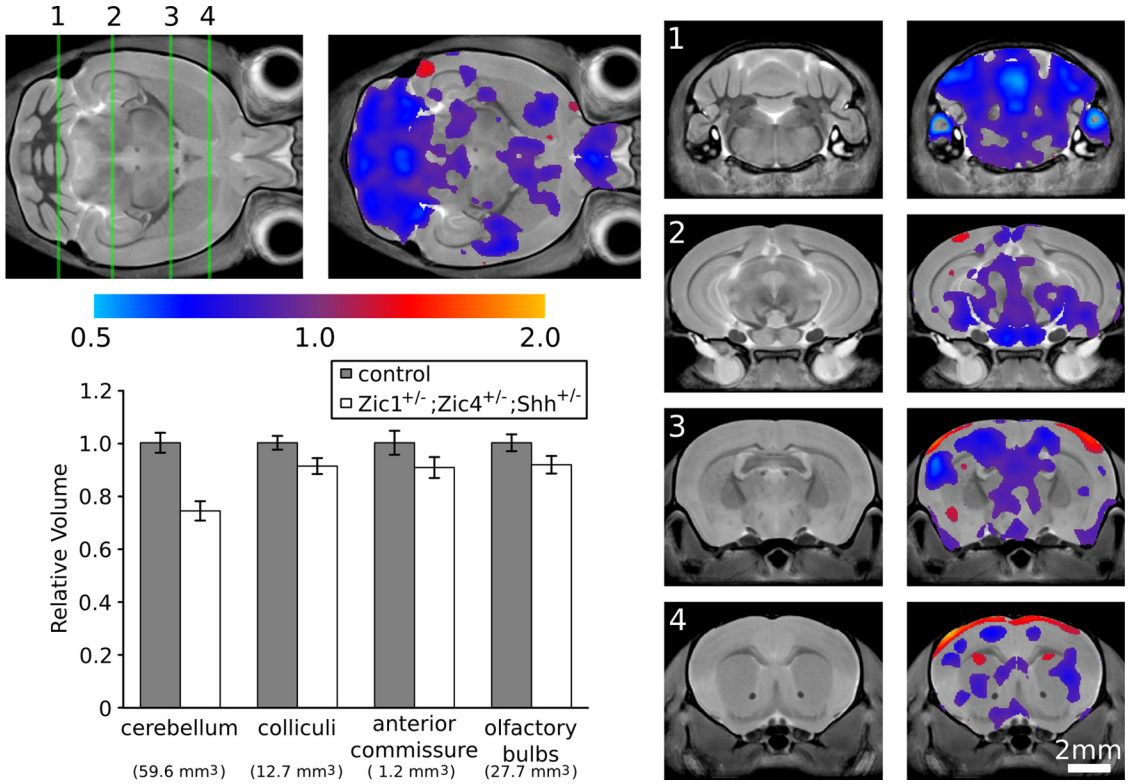

Fig. 3. MRI-detected brain phenotypes in the *Zic1*$^{+/-}$;*Zic4*$^{+/-}$;*Shh*$^{+/-}$ mouse. Voxelwise volumetric changes (where FDR <0.05) are shown overlaid on the unbiased average image (shown without overlay at *left* for each slice). Horizontal images (*top left*) include green lines indicating the location of the coronal slices (shown at *right*). Integration of voxelwise volume changes over segmented structure volumes provided a measure of volumetric changes. Thirty-seven (37) structures of the 63 tested showed significant differences (FDR <0.05). Four structures of interest are shown in the bar graph (*bottom left*) with error bars showing SE. Volumes are shown normalized to the control volume for each structure (shown in parentheses).

displacements mapping wild-type to mutant skulls, as well as the components of the displacements normal to and in the plane of the skull, showed significant differences in both mutants (Fig. 4). Morphological phenotypes were more widespread in the *Gja1*^{Jrt} mutant (modeling ODD), which showed particularly prominent changes in the facial region. The phenotype in the *Zic1*$^{+/-}$;*Zic4*$^{+/-}$;*Shh*$^{+/-}$ mutant (modeling DWM) was more localized and most noticeable at the posterior part of the skull in the region of the interparietal bone. In this case, the displacement was primarily in the plane of the skull and in the rostral-caudal direction.

Gja1^{Jrt} *and Zic1*$^{+/-}$;*Zic4*$^{+/-}$;*shh*$^{+/-}$ *brain and skull phenotypes correspond.* To compare the phenotype results obtained from the MRI and CT data, we registered MRI brain to micro-CT skull results via an affine registration (a mapping that includes three translations, three rotations, three scales, and three shears). The magnitude of deformations and the normal and in-plane displacements computed for the skull (as in Fig. 4) were also computed for the brain surface and then visualized after statistical thresholding. Visual comparison shows a high degree of correspondence in the brain and skull displacements in both cases (Fig. 5). The phenotype similarities are present in both magnitude and normal displacements and in the in-plane (rostral-caudal) displacements of the *Zic1*$^{+/-}$;*Zic4*$^{+/-}$;*Shh*$^{+/-}$. Two isolated regions showed small differences in the skull and brain phenotypes in the *Gja1*^{Jrt} in-plane data (Fig. 5*C*). The first region (identified by a green arrow in Fig. 5*C*) is on the lateral side of the skull and suggests a caudal shift in the CT skull data that is smaller in magnitude in the MRI data (and statistically significant over only a very small region). This appears in a flat, essentially two-dimensional, region of the skull surface where in-plane displacements may be more poorly constrained in the CT deformation analysis. The second difference, at the back of the brain and skull, highlights a mutant phenotype in which the caudal edge of the cerebellum is located more ventrally along the occipital plate in mutants compared with controls (as can be seen in Fig. 5*C*, *inset*).

To further investigate the brain-skull relationship, we tested the ability of brain surface displacements, brain structure volumes, and genotype, alone and in combination, to predict skull surface displacements. At the back of the head in the *Zic1*$^{+/-}$;*Zic4*$^{+/-}$;*Shh*$^{+/-}$ model of DWM, significant skull displacements of the interparietal bone were modeled as a function of corresponding brain surface displacements at the top of the cerebellum (Fig. 6, *left*) and as a function of total cerebellum volume (Fig. 6, *middle*). Each MRI measured parameter was significant independently; however, the addition of brain surface displacements or cerebellum volume to a model predicting skull displacements based on genotype alone (Fig. 6, *right*) did not provide a statistically significant improvement (P ~0.3 and 0.7 respectively, using an F-test for analysis of variance to compare fits). This proved to be the case for all voxels on the skull surface, indicating genotype is a better predictor of skull displacements than the local brain

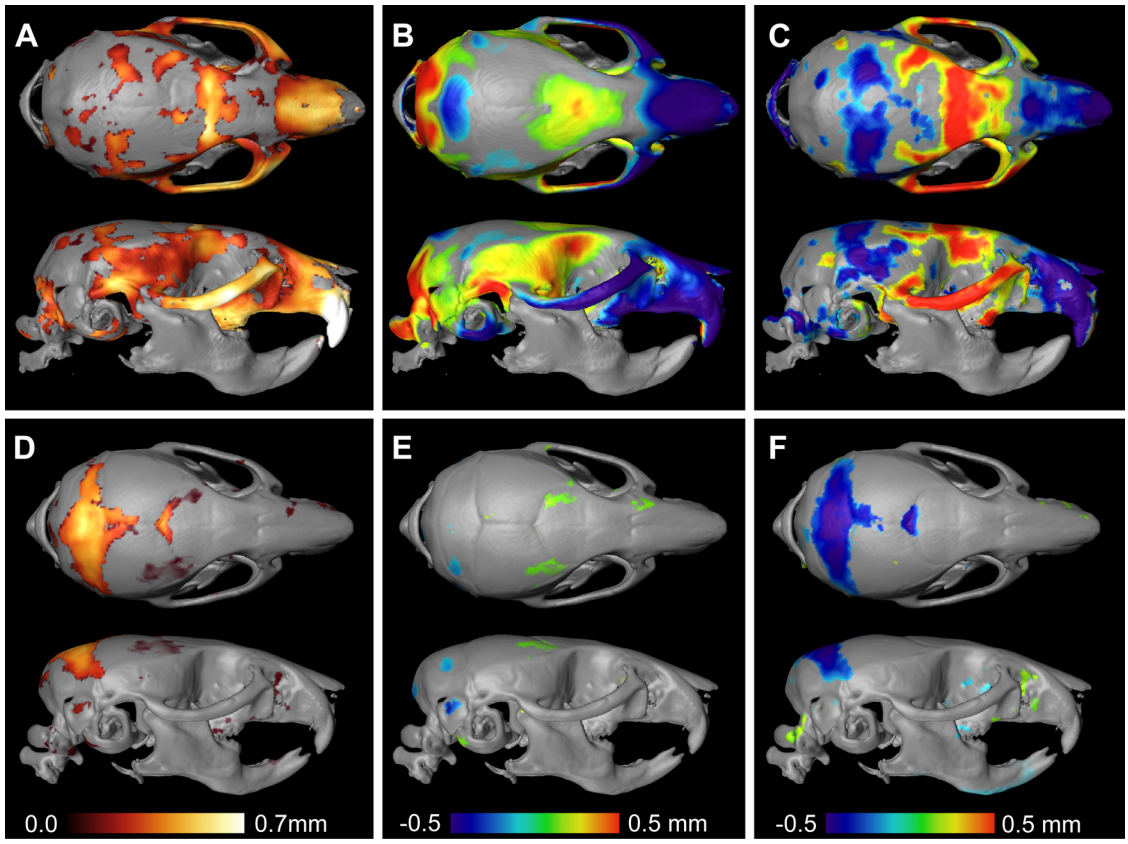

Fig. 4. CT skull phenotypes in *Gja1*^{Jrt} and *Zic1*$^{+/-}$;*Zic4*$^{+/-}$;*Shh*$^{+/-}$ mice. Both *Gja1*^{Jrt} (*A, B, C*) and *Zic1*$^{+/-}$;*Zic4*$^{+/-}$;*Shh*$^{+/-}$ (*D, E, F*) mice showed significant phenotypes in the shape of the skull. Visualizations of the mutant to wild-type differences are shown mapped onto the surface of the average skull image in regions where FDR <0.05. The magnitude of average vector displacements between the control and mutant mice are shown in *A* and *D*. Average displacements normal to the skull surface are shown in *B* and *E*, with positive defined in the extracranial direction. Average displacements both in the plane of the skull surface and in the sagittal plane (predominantly rostral-caudal in direction) are shown in *C* and *F*, with positive defined in the rostral direction. The differences were more widespread in the *Gja1*^{Jrt} mice, notably including large changes in the facial region (*A–C*). More localized changes were evident in *Zic1*$^{+/-}$;*Zic4*$^{+/-}$;*Shh*$^{+/-}$ mice (*D–F*), mostly in the vicinity of the interparietal bone and in the rostral-caudal (in-plane) direction (*F*).

structure measurements obtained with our methods. Identical analyses of the *Gja1*^{Jrt} mouse model of ODD showed similar results. Analyses modeling brain structure volumes by skull surface displacements would produce identical results (the directionality of the analysis is not meaningful).

We measured intracranial volume from skull data and compared this to the total brain volume measured from MRI data. Measurements from all genotypes (from both ODD and DWM mutants and their controls) are provided in Fig. 7*A*. Intracranial volume and total brain volume were highly correlated, with intracranial volume ~3% larger than the total brain volume (with 1% SE). As expected from such a close fit, and in contrast to the modeling of local skull displacements, total brain volume provided a better predictor of variations in total intracranial volume than did genotype, which provided no statistical improvement to intracranial volume estimates (P ~0.7). This observation was true when all genotypes were analyzed collectively (as in Fig. 7*A*) and when the *Gja1*^{Jrt} and *Zic1*$^{+/-}$;*Zic4*$^{+/-}$;*Shh*$^{+/-}$ genotypes were analyzed independently.

We further evaluated whether changes in shape might be dependent on overall size (an allometric relationship). As an example, in Fig. 7*B*, the volume ratio of the cerebellum to the whole brain is plotted as a function of the whole brain volume for the *Zic1*$^{+/-}$;*Zic4*$^{+/-}$;*Shh*$^{+/-}$ mice and their controls (modeling DWM). The use of the volume ratio removes linear dependence on size from measurements and generally reduces statistical variability (57). The plot would produce a smooth curve running through all genotypes for strictly allometric phenotypes. The sharp discontinuity between the genotypes evident in Fig. 7*B* instead indicates that the phenotype in the *Zic1*$^{+/-}$;*Zic4*$^{+/-}$;*Shh*$^{+/-}$ mice is much more prominent than any allometric relationship that might also be present.

DISCUSSION

The development of the brain and skull is a coordinated and sophisticated process that routinely results in a careful fit of one within the other. We have developed a combined MRI and CT analysis that allows a comparison of the geometries of the brain and skull in the mouse. Our results indicate that the brain and skull fit tightly together in each of the genotypes we examined. This tight fit is evident both from spatial maps of displacements on brain and skull surfaces, and from volumetric analyses showing the close correspondence between total brain and intracranial volumes. For the *Zic1*$^{+/-}$;*Zic4*$^{+/-}$;*Shh*$^{+/-}$ mouse model of DWM, this highlights a difference in the phenotype compared with the human case, in which the posterior fossa tends to be enlarged though the cerebellum is smaller (11). It is not possible from our data to determine if this

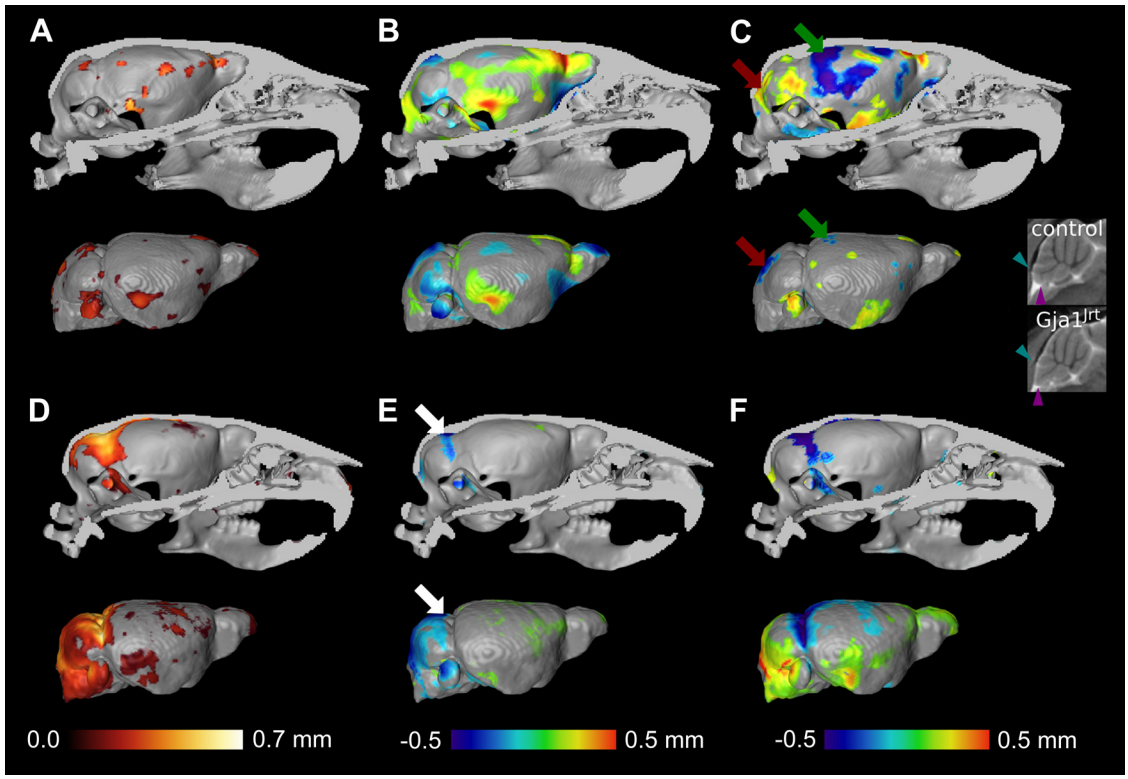

Fig. 5. Correspondence of MRI-brain and CT-skull phenotypes in *Gja1*^{Jrt} and *Zic1*$^{+/-}$;*Zic4*$^{+/-}$;*Shh*$^{+/-}$ mice. Visualization of the magnitude (*A, D*), normal (*B, E*) and in-plane (*C, F*) displacements on the intracranial skull surface (*top* of each panel) and on the brain surface (*bottom* of each panel) show that morphometric phenotypes in the skull and brain closely correspond. This correlation is evident in both the *Gja1*^{Jrt} (*A, B, C*) and *Zic1*$^{+/-}$;*Zic4*$^{+/-}$;*Shh*$^{+/-}$ (*D, E, F*) mutants. Positive directions are defined as extracranial (*B, E*) and rostral (*C, F*). The skull view is shown after removing one lateral half to enable view of the inside surface (the cut plane is colored a solid gray). In the *Zic1*$^{+/-}$;*Zic4*$^{+/-}$;*Shh*$^{+/-}$ mutant, close similarities between brain and skull phenotypes are evident in all panels (*D, E, F*). In the *Gja1*^{Jrt} mutant, the magnitudes displacements show little change (*A*, FDR <0.15 and FDR <0.10 for the CT and MR data, respectively) and the normal displacements closely correspond. Two differences in the skull and brain phenotypes appear on the in-plane displacements of the *Gja1*^{Jrt} mutant (*C*): on the lateral side of the skull (green arrows) the CT data suggests a caudal shift larger than is present in the MRI data; and at the caudal edge of the cerebellum (red arrows) the shift in the skull and brain are in opposite directions. The latter difference evidences a shift in the cerebellum relative to the skull, such that lobe IX (*inset C*, purple arrowheads) extends more ventrally from the edge of the occipital plate in the mutant (*inset C*, blue arrowheads). All colored regions in *B–F* are shown with FDR <0.05. White arrows (*E*) indicate the location of analysis plotted in Fig. 6.

difference in phenotype is related to an incomplete modeling of the genetic lesions in the DWM mouse model or to inherent differences in the brain between the mouse and human, notably including a disparate positioning of the cerebellum. It is important to note that the genotype used to model DWM for this analysis was in part a choice of convenience, since these mice are viable as adults. Our other DWM mouse models may be more likely to recapitulate the skull phenotype of human

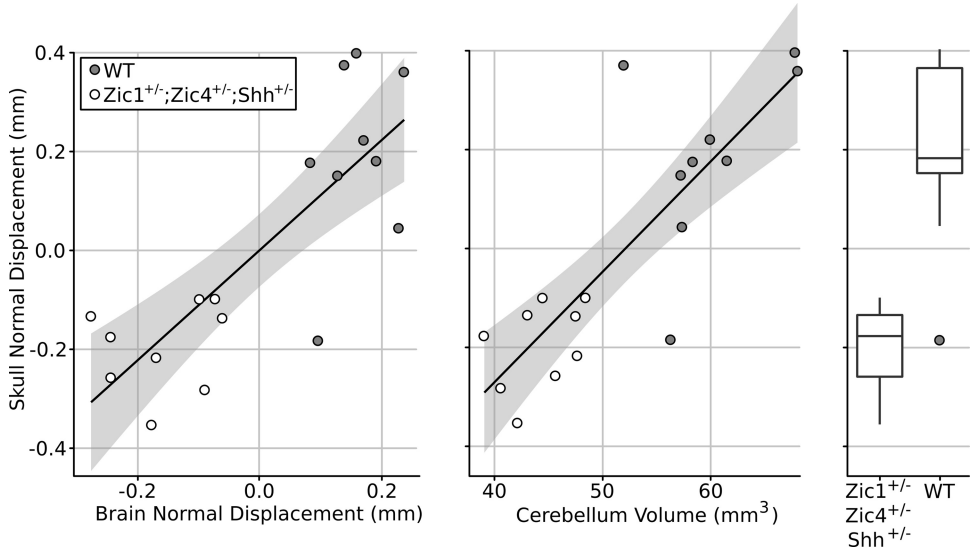

Fig. 6. Modeling CT-skull displacements by genotype, brain structure volume, and brain surface displacement in *Zic1*$^{+/-}$;*Zic4*$^{+/-}$;*Shh*$^{+/-}$ mice. Skull displacements were modeled as a function of brain surface displacements, brain structure volumes, and genotype. Although each independently showed significance, a model based solely on genotype was not improved by addition of MR-derived brain structure measurements. Lines of best fit are shown with 95% confidence intervals.

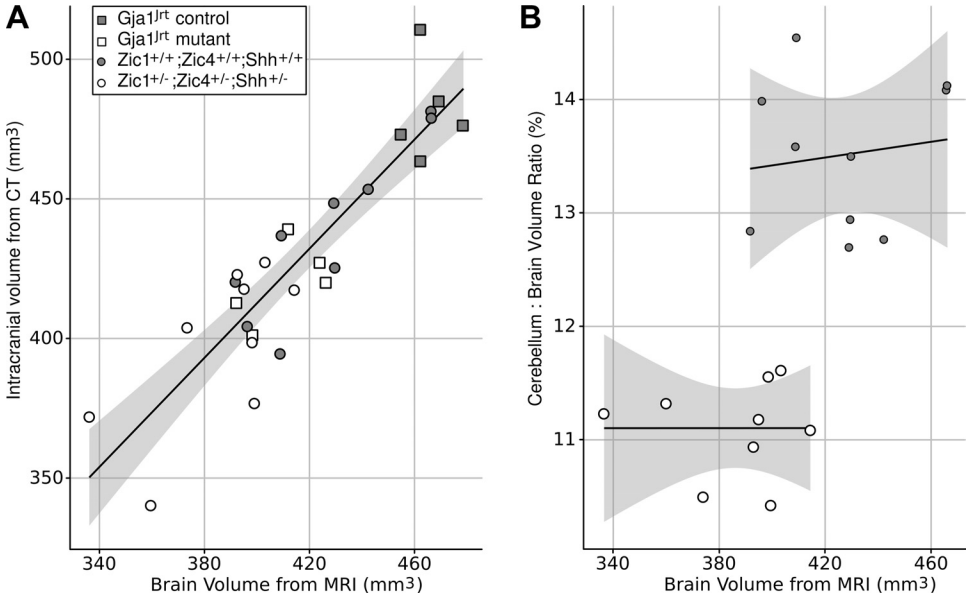

Fig. 7. Structure volume comparisons. In *A*, the intracranial skull volume as measured by CT is compared with the brain volume measured by MRI for all mice imaged in the study, showing the 2 measures are correlated ($R^2 = 0.8$). The correlation remained in both combined and separate analyses of *Gja1*^{Jrt} and *Zic1*$^{+/-}$;*Zic4*$^{+/-}$;*Shh*$^{+/-}$ mice (with their respective controls). In this case, MRI-derived brain volume was a stronger predictor of CT-derived intracranial volume than genotype. The line of best fit is shown with 95% confidence intervals. In *B*, the relative volume of the cerebellum is plotted vs. the whole brain volume for the *Zic1*$^{+/-}$;*Zic4*$^{+/-}$;*Shh*$^{+/-}$ mice and their controls. A line of best fit with 95% confidence intervals is shown for each genotype. The notable break between the 2 genotypes indicates that the differences in relative cerebellum size cannot be attributed to allometric differences (i.e., cannot be attributed to the differences in the overall brain size).

DWM; however, they are lethal prior to weaning, adding the complication of incomplete skull development (1, 15). Nonetheless, the analysis as demonstrated here provides a quantitative measure of the brain-skull phenotype relationships and will be useful in additional studies of mouse models of human conditions for identifying perturbations of the close fit between the brain and skull.

Both MRI and CT data proved to be sufficiently sensitive to detect phenotypes in the mouse models we examined here. It is worth noting two factors that affect the phenotype comparisons we made between the results. First, the CT skull images, in contrast to the MR images, consist largely of thin isointense bony plates and provide less local constraint for the volumetric registration procedures because of their two-dimensional character. This will allow more in-plane variability in the resulting deformation fields. In combination with other changes in the skull, this is a possible explanation for the CT and MR differences at the lateral side of the skull in the *Gja1*^{Jrt} mouse model of ODD. We note that this challenge is not unique to the deformation-based methods of comparison we use here and that it is conceptually equivalent to the requirement for "semilandmarks" in landmark-based methods of morphological analysis (74). Second, differences in statistical sensitivity are exacerbated by the statistical testing procedure we used here because the FDR correction for multiple comparisons becomes less stringent as more statistically significant voxels are detected. This is likely to produce somewhat larger statistically significant maps for some phenotypes and image modalities and explains the somewhat larger regions of significance on the *Zic1*$^{+/-}$;*Zic4*$^{+/-}$;*Shh*$^{+/-}$ brain surface compared with the inside skull surface (Fig. 5, *D–F*) because of the large number of significant voxels within the brain. With this acknowledgement of the differences in the nature of the CT and MRI data sets as well as the influence of the statistical testing procedure, the MRI and CT data show excellent correspondence of brain and skull phenotypes in both of the mouse models we examined.

Interestingly, genotype proved to be a better predictor of skull morphometry than did underlying brain features. This was true whether brain surface displacements or structure volumes were considered. On the other hand, we also found the intracranial volume was more effectively predicted by total brain volume than by genotype. Clearly, the local shapes of the brain and skull are highly genotype-dependent, but the total intracranial and brain volume also depend on several other factors affecting overall growth. The tight fit of the brain and skull was not disrupted in either of the genotypes we examined. It would be interesting in future experiments to explore the relative importance of genetic and physical factors during development on the final shape and size of the brain and skull in this context and to isolate genotypes where the brain and skull phenotypes separate to produce a much larger difference in brain and intracranial volumes.

In a similar way, more complete analysis of phenotype variability between genotypes and in individuals may provide insight into the physical and genotypic constraints affecting brain and skull development. A change in the phenotype variability of a particular genetically modified mouse strain would reflect a change in the degree of developmental control, even in the absence of phenotypic differences in the population average. It would be interesting to determine if a separation of brain and skull phenotypes also engenders an increase in the phenotype variability, which might provide insight into the role of physical vs. genetic interactions. We did not find significant differences between the structure volume variances in the mice in this study, even though both DWM and ODD are associated with a variable clinical presentation. It may be that a larger number of mice are required for this variability analysis, particularly in the *Gja1*^{Jrt} mice, or that the registration process itself contributes a nontrivial part of the variability observed. It is also possible that individual variation in particular mice reflects plasticity of structures within the brain, skull, or face. Although further experiments would be necessary to determine if our methods could detect plasticity associated with craniofacial development, morphological plasticity has already been demonstrated in the brains of adult mice (58). Thus, experiments comparing skull and brain phenotypes after manipula-

tion of environmental factors may allow one to probe the adaptability and variability of specific genotypes.

Developmental abnormalities in brain and skull morphology frequently appear together in the human population. In some cases, including craniosynostosis as an example, the two structures remain tightly fitted and the shapes remain closely related. In other cases, the close fit between the brain and skull may be lost. A notable example of the latter includes DWM and related conditions such as cerebellar vermis hypoplasia and megacisterna magna. Even in these cases though, other brain phenotype correlations may be noteworthy; DWM patients, for instance, can exhibit hypoplasia of the corpus callosum in addition to the cerebellum (10, 12). Cerebellar hypoplasia may also be associated with frontal lobe deficits, either evidenced by anatomical or behavioral changes (27). Similarly, in addition to characteristic changes in the shape of the face (92), the anterior cerebrum and cerebellum are affected in nonsyndromic cleft lip and palate (31, 93) and van der Woude syndrome (69) patients. Exploring these phenotype links in a broader range of relevant mouse models will reveal patterns inherently linked to the development process.

Relationships between the total volumes of the intracranial space and the brain are also of relevance in anthropology and evolution. Application of similar tools to the ones we describe here to a broader range of mouse genetic variants might be able to expand the correlative data in Fig. 7*A* and determine genetic factors affecting the modular development of the brain and skull. Morphological evaluations in the case of large phenotypic variations, such as between different species, may instead be best handled by landmark-based analysis. Results from a large population of genetically engineered mice with a range of phenotypes such as in a screen, however, could be efficiently obtained with our methods and have important implications for understanding mammalian developmental processes.

In a similar way, it would be interesting to determine if a combination of features within the mouse skull could be predictive of abnormalities within the mouse brain. Like the mice we examined here, mouse models of Apert syndrome and Down syndrome both show craniofacial and brain abnormalities (3, 7, 64, 78). Joint analysis in a number of different mouse models stands to elucidate which structures are developmentally linked. At least within a range of genetic variants and in closely related species, these phenotype linkages may not be limited to structures immediately adjacent to the skull, as correlation of skull features with more distant phenotypes is possible [analogous to phenotype correlations between the corpus callosum and the cerebellum (10, 12) and between the brain and face (69, 93) already mentioned].

The development of the brain and skull is a coordinated and sophisticated process that routinely results in a careful fit of one within the other. Disruption of this process is notable in several human conditions and appears to be affected by both genetic and physical factors. We have developed a combined MRI and CT analysis that allows a comparison of the geometries of the brain and skull in the mouse. We observed a close relationship between the morphological changes in these structures in two mouse mutants. This type of analysis will be useful for study of brain-skull relationships in mouse models of human conditions. In particular, we expect these methods in application to an appropriate group of mouse mutants will help provide a mechanistic understanding of abnormal craniofacial development, especially in cases where the close fit between the brain and skull becomes disrupted.

ACKNOWLEDGMENTS

The authors gratefully acknowledge the Centre for Modeling Human Disease for the *Gja1*^{Jrt} mouse.

GRANTS

Funding support was provided by the Ontario Institute for Cancer Research through funding from the Government of Ontario and by National Institutes of Health (NIH) Grant RO1NS-050386 (to K. J. Millen). R. M. Henkelman is recipient of a Canada Research Chair in Imaging. M. C. Blank is recipient of NIH Training Grant T32GM-007183.

DISCLOSURES

No conflicts of interest, financial or otherwise, are declared by the author(s).

AUTHOR CONTRIBUTIONS

Author contributions: B.J.N., M.C.B., R.M.H., and K.J.M. conception and design of research; B.J.N., M.C.B., and B.B.R. performed experiments; B.J.N., R.M.H., and K.J.M. analyzed data; B.J.N., R.M.H., and K.J.M. interpreted results of experiments; B.J.N. prepared figures; B.J.N. drafted manuscript; B.J.N., R.M.H., and K.J.M. edited and revised manuscript; B.J.N., R.M.H., and K.J.M. approved final version of manuscript.

REFERENCES

1. **Aldinger KA, Lehmann OJ, Hudgins L, Chizhikov VV, Bassuk AG, Ades LC, Krantz ID, Dobyns WB, Millen KJ.** FOXC1 is required for normal cerebellar development and is a major contributor to chromosome 6p25.3 Dandy-Walker malformation. *Nat Genet* 41: 1037–1042, 2009.
2. **Aldridge K, George ID, Cole KK, Austin JR, Takahashi TN, Duan Y, Miles JH.** Facial phenotypes in subgroups of prepubertal boys with autism spectrum disorders are correlated with clinical phenotypes. *Mol Autism* 2: 15, 2011.
3. **Aldridge K, Hill CA, Austin JR, Percival C, Martinez-Abadias N, Neuberger T, Wang Y, Jabs EW, Richtsmeier JT.** Brain phenotypes in two FGFR2 mouse models for Apert syndrome. *Dev Dyn* 239: 987–997, 2010.
4. **Aldridge K, Kane AA, Marsh JL, Panchal J, Boyadjiev SA, Yan P, Govier D, Ahmad W, Richtsmeier JT.** Brain morphology in nonsyndromic unicoronal craniosynostosis. *Anat Rec A Discov Mol Cell Evol Biol* 285: 690–698, 2005.
5. **Aldridge K, Kane AA, Marsh JL, Yan P, Govier D, Richtsmeier JT.** Relationship of brain and skull in pre- and postoperative sagittal synostosis. *J Anat* 206: 373–385, 2005.
6. **Aldridge K, Marsh JL, Govier D, Richtsmeier JT.** Central nervous system phenotypes in craniosynostosis. *J Anat* 201: 31–39, 2002.
7. **Aldridge K, Reeves RH, Olson LE, Richtsmeier JT.** Differential effects of trisomy on brain shape and volume in related aneuploid mouse models. *Am J Med Genet A* 143A: 1060–1070, 2007.
8. **Anthony B, Vinci-Booher S, Wetherill L, Ward R, Goodlett C, Zhou FC.** Alcohol-induced facial dysmorphology in C57BL/6 mouse models of fetal alcohol spectrum disorder. *Alcohol* 44: 659–671, 2010.
9. **Armstrong E, Zilles K, Curtis M, Schleicher A.** Cortical folding, the lunate sulcus and the evolution of the human brain. *J Hum Evol* 20: 341–348, 1991.
10. **Asai A, Hoffman HJ, Hendrick EB, Humphreys RP.** Dandy-Walker syndrome: experience at the Hospital for Sick Children, Toronto. *Pediatr Neurosci* 15: 66–73, 1989.
11. **Barkovich AJ, Millen KJ, Dobyns WB.** A developmental and genetic classification for midbrain-hindbrain malformations. *Brain* 132: 3199–3230, 2009.
12. **Barkovich AJ, Norman D.** Anomalies of the corpus callosum: correlation with further anomalies of the brain. *AJR Am J Roentgenol* 151: 171–179, 1988.
13. **Bastir M, Rosas A, O'higgins P.** Craniofacial levels and the morphological maturation of the human skull. *J Anat* 209: 637–654, 2006.
14. **Benjamini Y, Hochberg Y.** Controlling the false discovery rate: a practical and powerful approach to multiple testing. *J Roy Stat Soc B* 57: 289–300, 1995.

15. **Blank MC, Grinberg I, Aryee E, Laliberte C, Chizhikov VV, Henkelman RM, Millen KJ.** Multiple developmental programs are altered by loss of Zic1 and Zic4 to cause Dandy-Walker malformation cerebellar pathogenesis. *Development* 138: 1207–1216, 2011.
16. **Boughner JC, Wat S, Diewert VM, Young NM, Browder LW, Hallgrímsson B.** Short-faced mice and developmental interactions between the brain and the face. *J Anat* 213: 646–662, 2008.
17. **Bruner E, Holloway RL.** A bivariate approach to the widening of the frontal lobes in the genus Homo. *J Hum Evol* 58: 138–146, 2010.
18. **Bruner E, Manzi G.** Landmark-based shape analysis of the archaic Homo calvarium from Ceprano (Italy). *Am J Phys Anthropol* 132: 355–366, 2007.
19. **Bruner E, Manzi G, Arsuaga JL.** Encephalization and allometric trajectories in the genus homo: evidence from the neandertal and modern lineages. *Proc Natl Acad Sci USA* 100: 15335–15340, 2003.
20. **Bruner E, Martin-Loeches M, Burgaleta M, Colom R.** Midsagittal brain shape correlation with intelligence and cognitive performance. *Intelligence* 39: 141–147, 2011.
21. **Cao J, Worsley KJ.** The detection of local shape changes via the geometry of Hotelling's T2 fields. *Ann Stat* 27: 925–942, 1999.
22. **Carroll JB, Lerch JP, Franciosi S, Spreeuw A, Bissada N, Henkelman RM, Hayden MR.** Natural history of disease in the YAC128 mouse reveals a discrete signature of pathology in Huntington disease. *Neurobiol Dis* 43: 257–265, 2011.
23. **Chen XJ, Kovacevic N, Lobaugh NJ, Sled JG, Henkelman RM, Henderson JT.** Neuroanatomical differences between mouse strains as shown by high-resolution 3D MRI. *Neuroimage* 29: 99–105, 2006.
24. **Chernoff GF.** The fetal alcohol syndrome in mice: an animal model. *Teratology* 15: 223–229, 1977.
25. **Cheverud J, Lewis JL, Bachrach W, Lew WD.** The measurement of form and variation in form: an application of three-dimensional quantitative morphology by finite-element methods. *Am J Phys Anthropol* 62: 151–165, 1983.
26. **Cheverud JM.** Quantitative genetic analysis of cranial morphology in the cotton-top (Saguinus oedipus) and saddle-back (S. fuscicollis) tamarins. *J Evolut Biol* 9: 5–42, 1996.
27. **Ciesielski KT, Harris RJ, Hart BL, Pabst HF.** Cerebellar hypoplasia and frontal lobe cognitive deficits in disorders of early childhood. *Neuropsychologia* 35: 643–655, 1997.
28. **Clarren SK, Alvord EC, Sumi SM, Streissguth AP, Smith DW.** Brain malformations related to prenatal exposure to ethanol. *J Pediatr* 92: 64–67, 1978.
29. **Clarren SK, Smith DW.** The fetal alcohol syndrome. *N Engl J Med* 298: 1063–1067, 1978.
30. **Collins DL, Neelin P, Peters TM, Evans AC.** Automatic 3D intersubject registration of MR volumetric data in standardized Talairach space. *J Comput Assist Tomogr* 18: 192–205, 1994.
31. **Conrad AL, Dailey S, Richman L, Canady J, Karnell MP, Axelson E, Nopoulos P.** Cerebellum structure differences and relationship to speech in boys and girls with nonsyndromic cleft of the lip and/or palate. *Cleft Palate Craniofac J* 47: 469–475, 2010.
32. **Conroy GC, Falk D, Guyer J, Weber GW, Seidler H, Recheis W.** Endocranial capacity in Sts 71 (Australopithecus africanus) by three-dimensional computed tomography. *Anat Rec* 258: 391–396, 2000.
33. **Demyer W, Zeman W, Palmer CG.** The face predicts the brain: diagnostic significance of median facial anomalies for holoprosencephaly (arhinencephaly). *Pediatrics* 34: 256–263, 1964.
34. **Dorr AE, Lerch JP, Spring S, Kabani N, Henkelman RM.** High resolution three-dimensional brain atlas using an average magnetic resonance image of 40 adult C57Bl/6J mice. *Neuroimage* 42: 60–69, 2008.
35. **Ellegood J, Lerch JP, Henkelman RM.** Brain abnormalities in a Neuroligin3 R451C knockin mouse model associated with autism. *Autism Res* 4: 368–376, 2011.
36. **Falk D, Clarke R.** Brief communication: new reconstruction of the Taung endocast. *Am J Phys Anthropol* 134: 529–534, 2007.
37. **Falk D, Hildebolt C, Smith K, Morwood MJ, Sutikna T, Brown P, Jatmiko, Saptomo EW, Brunsden B, Prior F.** The brain of LB1, Homo floresiensis. *Science* 308: 242–245, 2005.
38. **Falk D, Hildebolt C, Smith K, Morwood MJ, Sutikna T, Jatmiko Saptomo EW, Imhof H, Seidler H, Prior F.** Brain shape in human microcephalics and Homo floresiensis. *Proc Natl Acad Sci USA* 104: 2513–2518, 2007.
39. **Falk D, Hildebolt C, Smith K, Morwood MJ, Sutikna T, Jatmiko Wayhu Saptomo E, Prior F.** LB1's virtual endocast, microcephaly, and hominin brain evolution. *J Hum Evol* 57: 597–607, 2009.
40. **Flenniken AM, Osborne LR, Anderson N, Ciliberti N, Fleming C, Gittens JE, Gong XQ, Kelsey LB, Lounsbury C, Moreno L, Nieman BJ, Peterson K, Qu D, Roscoe W, Shao Q, Tong D, Veitch GI, Voronina I, Vukobradovic I, Wood GA, Zhu Y, Zirngibl RA, Aubin JE, Bai D, Bruneau BG, Grynpas M, Henderson JE, Henkelman RM, McKerlie C, Sled JG, Stanford WL, Laird DW, Kidder GM, Adamson SL, Rossant J.** A Gja1 missense mutation in a mouse model of oculodentodigital dysplasia. *Development* 132: 4375–4386, 2005.
41. **Franklin D, Freedman L, Milne N, Oxnard CE.** Geometric morphometric study of population variation in indigenous southern African crania. *Am J Hum Biol* 19: 20–33, 2007.
42. **Genovese CR, Lazar NA, Nichols T.** Thresholding of statistical maps in functional neuroimaging using the false discovery rate. *Neuroimage* 15: 870–878, 2002.
43. **Grinberg I, Northrup H, Ardinger H, Prasad C, Dobyns WB, Millen KJ.** Heterozygous deletion of the linked genes ZIC1 and ZIC4 is involved in Dandy-Walker malformation. *Nat Genet* 36: 1053–1055, 2004.
44. **Hallgrímsson B, Dorval CJ, Zelditch ML, German RZ.** Craniofacial variability and morphological integration in mice susceptible to cleft lip and palate. *J Anat* 205: 501–517, 2004.
45. **Hallgrímsson B, Lieberman DE.** Mouse models and the evolutionary developmental biology of the skull. *Integr Comp Biol* 48: 373–384, 2008.
46. **Hallgrímsson B, Lieberman DE, Liu W, Ford-Hutchinson AF, Jirik FR.** Epigenetic interactions and the structure of phenotypic variation in the cranium. *Evol Dev* 9: 76–91, 2007.
47. **Holloway RL.** Revisiting the South African Taung australopithecine endocast: The position of the lunate sulcus as determined by the stereoplotting technique. *Am J Phys Anthropol* 56: 43–58, 1981.
48. **Holloway RL.** Cerebral brain endocast pattern of Australopithecus afarensis hominid. *Nature* 303: 420–422, 1983.
49. **Holloway RL.** The failure of the gyrification index (GI) to account for volumetric reorganization in the evolution of the human brain. *J Hum Evol* 22: 163–170, 1992.
50. **Holloway RL Jr.** Cranial capacity, neural reorganization, and hominid evolution: a search for more suitable parameters. *Am Anthropol* 68: 103–121, 1966.
51. **Hukki J, Saarinen P, Kangasniemi M.** Single suture craniosynostosis: diagnosis and imaging. *Front Oral Biol* 12: 79–90, 2008.
52. **Juriloff DM, Harris MJ.** Mouse genetic models of cleft lip with or without cleft palate. *Birth Defects Res A Clin Mol Teratol* 82: 63–77, 2008.
53. **Klingenberg CP.** Heterochrony and allometry: the analysis of evolutionary change in ontogeny. *Biol Rev Camb Philos Soc* 73: 79–123, 1998.
54. **Klingenberg CP.** Evolution and development of shape: integrating quantitative approaches. *Nat Rev Genet* 11: 623–635, 2010.
55. **Kovaceví N, Henderson JT, Chan E, Lifshitz N, Bishop J, Evans AC, Henkelman RM, Chen XJ.** A three-dimensional MRI atlas of the mouse brain with estimates of the average and variability. *Cereb Cortex* 15: 639–645, 2005.
56. **Lerch JP, Carroll JB, Dorr A, Spring S, Evans AC, Hayden MR, Sled JG, Henkelman RM.** Cortical thickness measured from MRI in the YAC128 mouse model of Huntington's disease. *Neuroimage* 41: 243–251, 2008.
57. **Lerch JP, Gazdzinski L, Germann J, Sled JG, Henkelman RM, Nieman BJ.** Wanted dead or alive? The tradeoff between in-vivo versus ex-vivo MR brain imaging in the mouse. *Front Neuroinform* 6: 6, 2012.
58. **Lerch JP, Yiu AP, Martinez-Canabal A, Pekar T, Bohbot VD, Frankland PW, Henkelman RM, Josselyn SA, Sled JG.** Maze training in mice induces MRI-detectable brain shape changes specific to the type of learning. *Neuroimage* 54: 2086–2095, 2011.
59. **Lieberman DE, Hallgrímsson B, Liu W, Parsons TE, Jamniczky HA.** Spatial packing, cranial base angulation, and craniofacial shape variation in the mammalian skull: testing a new model using mice. *J Anat* 212: 720–735, 2008.
60. **Majewski F.** Alcohol embryopathy: some facts and speculations about pathogenesis. *Neurobehav Toxicol Teratol* 3: 129–144, 1981.
61. **Marcucio RS, Young NM, Hu D, Hallgrimsson B.** Mechanisms that underlie co-variation of the brain and face. *Genesis* 49: 177–189, 2011.

62. **Martin RD, Maclarnon AM, Phillips JL, Dobyns WB.** Flores hominid: new species or microcephalic dwarf? *Anat Rec A Discov Mol Cell Evol Biol* 288: 1123–1145, 2006.
63. **Martínez-Abadías N, Heuzé Y, Wang Y, Jabs EW, Aldridge K, Richtsmeier JT.** FGF/FGFR signaling coordinates skull development by modulating magnitude of morphological integration: evidence from Apert syndrome mouse models. *PLoS One* 6: e26425, 2011.
64. **Martínez-Abadías N, Percival C, Aldridge K, Hill CA, Ryan T, Sirivunnabood S, Wang Y, Jabs EW, Richtsmeier JT.** Beyond the closed suture in Apert syndrome mouse models: evidence of primary effects of FGFR2 signaling on facial shape at birth. *Dev Dyn* 239: 3058–3071, 2010.
65. **Murray SA.** Mouse resources for craniofacial research. *Genesis* 49: 190–199, 2011.
66. **Neubauer S, Gunz P, Hublin JJ.** The pattern of endocranial ontogenetic shape changes in humans. *J Anat* 215: 240–255, 2009.
67. **Neubauer S, Gunz P, Hublin JJ.** Endocranial shape changes during growth in chimpanzees and humans: a morphometric analysis of unique and shared aspects. *J Hum Evol* 59: 555–566, 2010.
68. **Nieman BJ, Flenniken AM, Adamson SL, Henkelman RM, Sled JG.** Anatomical phenotyping in the brain and skull of a mutant mouse by magnetic resonance imaging and computed tomography. *Physiol Genomics* 24: 154–162, 2006.
69. **Nopoulos P, Richman L, Andreasen NC, Murray JC, Schutte B.** Abnormal brain structure in adults with Van der Woude syndrome. *Clin Genet* 71: 511–517, 2007.
70. **O'Leary-Moore SK, Parnell SE, Godin EA, Dehart DB, Ament JJ, Khan AA, Johnson GA, Styner MA, Sulik KK.** Magnetic resonance microscopy-based analyses of the brains of normal and ethanol-exposed fetal mice. *Birth Defects Res A Clin Mol Teratol* 88: 953–964, 2010.
71. **Panchal J, Uttchin V.** Management of craniosynostosis. *Plast Reconstr Surg* 111: 2032–2048, 2003.
72. **Parsons TE, Kristensen E, Hornung L, Diewert VM, Boyd SK, German RZ, Hallgrímsson B.** Phenotypic variability and craniofacial dysmorphology: increased shape variance in a mouse model for cleft lip. *J Anat* 212: 135–143, 2008.
73. **Parsons TE, Schmidt EJ, Boughner JC, Jamniczky HA, Marcucio RS, Hallgrímsson B.** Epigenetic integration of the developing brain and face. *Dev Dyn* 240: 2233–2244, 2011.
74. **Perez SI, Bernal V, Gonzalez PN.** Differences between sliding semi-landmark methods in geometric morphometrics, with an application to human craniofacial and dental variation. *J Anat* 208: 769–784, 2006.
75. **Radinsky L.** Allometry and reorganization in horse skull proportions. *Science* 221: 1189–1191, 1983.
76. **Richman JM, Tickle C.** Epithelial-mesenchymal interactions in the outgrowth of limb buds and facial primordia in chick embryos. *Dev Biol* 154: 299–308, 1992.
77. **Richtsmeier JT, Aldridge K, DeLeon VB, Panchal J, Kane AA, Marsh JL, Yan P, Cole TM.** Phenotypic integration of neurocranium and brain. *J Exp Zool B Mol Dev Evol* 306: 360–378, 2006.
78. **Richtsmeier JT, Baxter LL, Reeves RH.** Parallels of craniofacial maldevelopment in Down syndrome and Ts65Dn mice. *Dev Dyn* 217: 137–145, 2000.
79. **Rogers SW.** Exploring dinosaur neuropaleobiology: viewpoint computed tomography scanning and analysis of an Allosaurus fragilis endocast. *Neuron* 21: 673–679, 1998.
80. **Rosas A, Bastir M.** Thin-plate spline analysis of allometry and sexual dimorphism in the human craniofacial complex. *Am J Phys Anthropol* 117: 236–245, 2002.
81. **Ross C, Henneberg M.** Basicranial flexion, relative brain size, and facial kyphosis in Homo sapiens and some fossil hominids. *Am J Phys Anthropol* 98: 575–593, 1995.
82. **Ross CF, Ravosa MJ.** Basicranial flexion, relative brain size, and facial kyphosis in nonhuman primates. *Am J Phys Anthropol* 91: 305–324, 1993.
83. **Roussotte FF, Sulik KK, Mattson SN, Riley EP, Jones KL, Adnams CM, May PA, O'Connor MJ, Narr KL, Sowell ER.** Regional brain volume reductions relate to facial dysmorphology and neurocognitive function in fetal alcohol spectrum disorders. *Hum Brain Mapp* 33: 920–937, 2012.
84. **Schmidt EJ, Parsons TE, Jamniczky HA, Gitelman J, Trpkov C, Boughner JC, Logan CC, Sensen CW, Hallgrímsson B.** Micro-computed tomography-based phenotypic approaches in embryology: procedural artifacts on assessments of embryonic craniofacial growth and development. *BMC Dev Biol* 10: 18, 2010.
85. **Schneider RA, Hu D, Helms JA.** From head to toe: conservation of molecular signals regulating limb and craniofacial morphogenesis. *Cell Tissue Res* 296: 103–109, 1999.
86. **Singh N, Harvati K, Hublin JJ, Klingenberg CP.** Morphological evolution through integration: a quantitative study of cranial integration in Homo, Pan, Gorilla and Pongo. *J Hum Evol* 62: 155–164, 2012.
87. **Spring S, Lerch JP, Henkelman RM.** Sexual dimorphism revealed in the structure of the mouse brain using three-dimensional magnetic resonance imaging. *Neuroimage* 35: 1424–1433, 2007.
88. **Spring S, Lerch JP, Wetzel MK, Evans AC, Henkelman RM.** Cerebral asymmetries in 12-week-old C57Bl/6J mice measured by magnetic resonance imaging. *Neuroimage* 50: 409–415, 2010.
89. **Sulik KK, Johnston MC.** Sequence of developmental alterations following acute ethanol exposure in mice: craniofacial features of the fetal alcohol syndrome. *Am J Anat* 166: 257–269, 1983.
90. **Vannucci RC, Barron TF, Holloway RL.** Craniometric ratios of microcephaly and LB1, Homo floresiensis, using MRI and endocasts. *Proc Natl Acad Sci USA* 108: 14043–14048, 2011.
91. **Verdyck P, Wuyts W, Van Hul W.** Genetic defects in the development of the skull vault in humans and mice. *Crit Rev Eukaryot Gene Expr* 16: 119–142, 2006.
92. **Ward RE, Moore ES, Hartsfield JK.** Morphometric characteristics of subjects with oral facial clefts and their relatives, In: *Cleft Lip and Palate: From Origin to Treatment*, edited by Wyszynski DF. New York: Oxford University Press, 2002.
93. **Weinberg SM, Andreasen NC, Nopoulos P.** Three-dimensional morphometric analysis of brain shape in nonsyndromic orofacial clefting. *J Anat* 214: 926–936, 2009.
94. **de Winter W, Oxnard CE.** Evolutionary radiations and convergences in the structural organization of mammalian brains. *Nature* 409: 710–714, 2001.
95. **Yang Y, Roussotte F, Kan E, Sulik KK, Mattson SN, Riley EP, Jones KL, Adnams CM, May PA, O'Connor MJ, Narr KL, Sowell ER.** Abnormal cortical thickness alterations in fetal alcohol spectrum disorders and their relationships with facial dysmorphology. *Cereb Cortex* 22: 1170–1179, 2012.
96. **Yin L, Du X, Li C, Xu X, Chen Z, Su N, Zhao L, Qi H, Li F, Xue J, Yang J, Jin M, Deng C, Chen L.** A Pro253Arg mutation in fibroblast growth factor receptor 2 (Fgfr2) causes skeleton malformation mimicking human Apert syndrome by affecting both chondrogenesis and osteogenesis. *Bone* 42: 631–643, 2008.
97. **Young DL, Schneider RA, Hu D, Helms JA.** Genetic and teratogenic approaches to craniofacial development. *Crit Rev Oral Biol Med* 11: 304–317, 2000.
98. **Yu X, Nieman BJ, Sudarov A, Szulc KU, Abdollahian DJ, Bhatia N, Lalwani AK, Joyner AL, Turnbull DH.** Morphological and functional midbrain phenotypes in Fibroblast Growth Factor 17 mutant mice detected by Mn-enhanced MRI. *Neuroimage* 56: 1251–1258, 2011.
99. **Zelditch ML.** Ontogenetic variation in patterns of phenotypic integration in the laboratory rat. *Evolution* 42: 28–41, 1988.
100. **Zelditch ML, Lundrigan BL, Garland T.** Developmental regulation of skull morphology. I. Ontogenetic dynamics of variance. *Evol Dev* 6: 194–206, 2004.
101. **Zelditch ML, Mezey J, Sheets HD, Lundrigan BL, Garland T.** Developmental regulation of skull morphology II: ontogenetic dynamics of covariance. *Evol Dev* 8: 46–60, 2006.
102. **Zhou YQ, Davidson L, Henkelman RM, Nieman BJ, Foster FS, Yu LX, Chen XJ.** Ultrasound-guided left-ventricular catheterization: a novel method of whole mouse perfusion for microimaging. *Lab Invest* 84: 385–389, 2004.